**Supporting Information**

# Designing vertical channels with expanded interlayer for Li-ion batteries

Long Zhang, Yunmei Pan, Yufei Chen, Mengxiong Li, Peiying Liu, Cancan Wang, Peng Wang, and Hongbin Lu*

State Key Laboratory of Molecular Engineering of Polymers, Department of Macromolecular Science, Collaborative Innovation Center of Polymers and Polymer Composites, Fudan University, 2005 Songhu Road, Shanghai 200438, China.
E-mail: hongbinlu@fudan.edu.cn

## Experimental

### Synthesis of MoS$_2$/Gr/C composite

Graphene oxide (GO) was prepared by modified Hummers method. MoS$_2$/Gr/C composite was synthesized by one-step solvent thermal method followed by annealing. Firstly, 60 mg of GO was added to 30 mL ethylene glycol, and then GO solution was obtained by ultrasonic dispersion for 30 min. In the ultrasonic process, a few drops of deionized water were added to assist the dispersion. Next, 200 mg of thiourea, 200 mg of ammonium molybdate, 100 μL of pyrrole, and 100 μL of octylame were added into the GO solution with stirring to form a homogeneous solution. Then, the solution was transferred into a 100ml high pressure reactor and put into an oven with a temperature of 200 ℃ for 12 hours. After cooling to room temperature, the intermediate products were washed to neutral with deionized water and dried at 60 °C under vacuum. Finally, the dried samples were annealed at 800 ℃ in N$_2$ for 2 h with a heating rate of 5 °C/min, and the MoS$_2$/graphene/carbon composite (MoS$_2$/Gr/C) was obtained. As the control group, MoS$_2$/C and MoS$_2$/Gr composites were synthesized with the similar method, without addition of GO or carbon source, respectively. MoS$_2$/C+Gr was synthesized via mechanical mixing the MoS$_2$/C composite and commercial graphene (The Sixth Element Inc.) in proportion.

### Characterization

The crystal structures of samples were characterized by X -ray diffraction (XRD) using a PANalytical X'Pert PRO diffractometer with Cu K$_\alpha$ radiation (λ = 1.54 Å) and operating at 40 kV and 40 mA. The morphology and structure of the samples were

observed by field emission scanning electron microscopy (FESEM, Ultra 55), transmission electron microscopy (TEM, Tecnai G2 20 TWIN) and high-resolution TEM (HRTEM, JEM-2100F). The elemental composition and chemical state were studied by X-ray photoelectron spectroscopy (XPS), using an AXIS UltraDLD spectrometer (Shimadzu-Kratos). The Raman spectrum was investigated with a Raman spectroscope (excitation wavelength 532 nm, XploRA, HORIBA JobinYvon). Thermogravimetric analysis (TGA, Pyris1) was conducted under air flow with a heating rate of 10 °C min$^{-1}$ from 50 to 600 °C.

**Electrochemical measurements**

Electrochemical properties of $MoS_2/Gr/C$ and $MoS_2/C$ composites were evaluated using coin-type cells (CR2016). For cell assembly, 70 wt% active materials, 20 wt% acetylene black, and 10 wt% polyvinylidene fluoride (PVDF) binder were mixed in Nmethyl-2-pyrrolidone (NMP) to form a uniform slurry. Then the slurry was coated onto a Copper foil and dried at 90 °C under vacuum with mass loading of ~1.0 mg cm$^{-2}$. The CR2016 coin cells were assembled in a glove box full of argon gas (the contents of oxygen and moisture ＜ 0.1 ppm) using the coated Cu foil as cathode, a lithium metal as anode, and a Celgard 2400 membrane as separator. The electrolyte was 1 M $LiPF_6$ in ethylene carbonate/diethyl carbonate (1:1 by volume) solution. Galvanostatic discharge/charge tests were conducted on a battery testing instrument (Land CT2001A, Wuhan China) in the voltage range 0.01–3 V (vs. Li$^+$/Li). Cyclic voltammetry (CV) curves were recorded with an IVIUM-n-STAT electrochemical workstation (Ivium Technologies, Netherlands) in the voltage range of 0.01–3 V (vs. Li$^+$/Li).

Electrochemical impedance spectra (EIS) were obtained on a CHI 660E electrochemical workstation with an amplitude of 5 mV, and from 100 kHz to 0.1 Hz at open circuit potential.
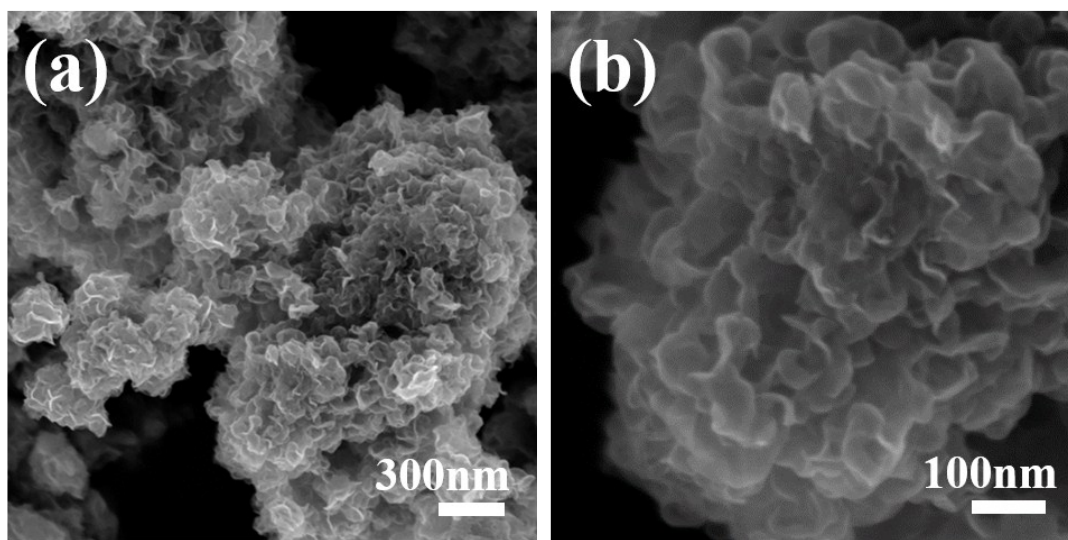


**Fig. S1** (a, b) FESEM images of the $MoS_2$/C composite at different magnifications.
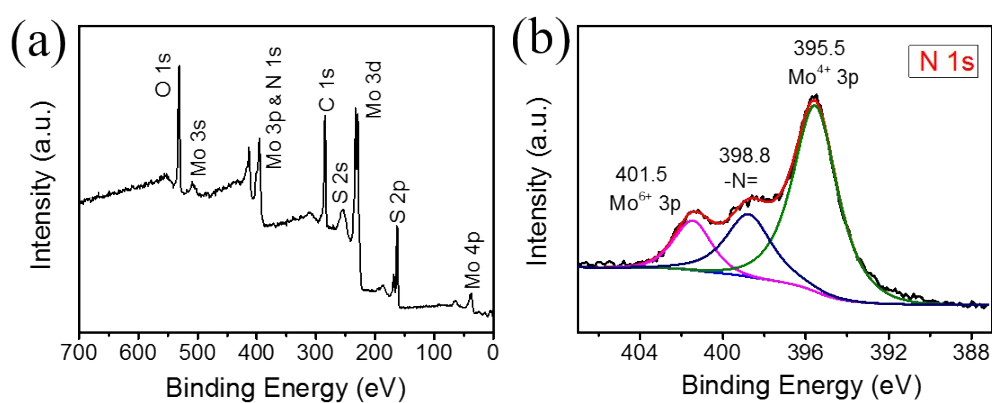


**Fig. S2** (a) The full XPS survey spectrum of the $MoS_2$/Gr/C composite, containing elements Mo, S, O, C and N. (b) The high-resolution N 1s spectrum of the $MoS_2$/Gr/C composite.
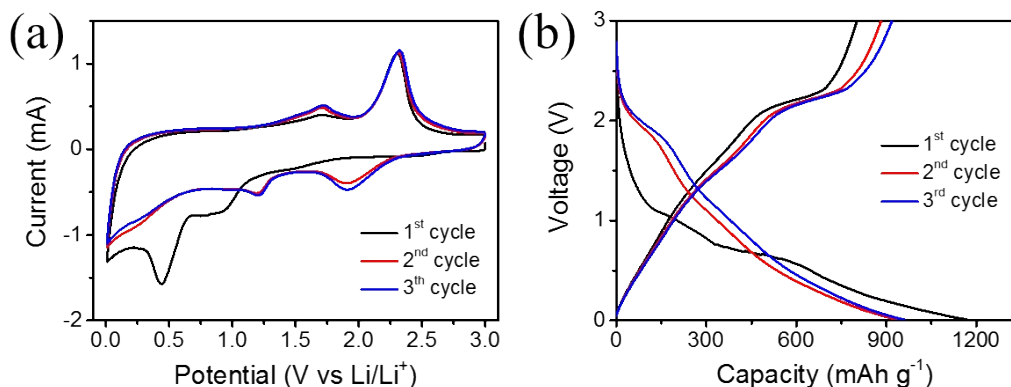
**Fig. S3** (a) CV curves of the $MoS_2/Gr/C$ electrode at scan rate of 0.5 mV s$^{-1}$ with the voltage range of 0.01–3.0 V for the initial three cycles. (b) The discharge/charge curves of the $MoS_2/Gr/C$ at 0.2 A g$^{-1}$ for the initial three cycles.
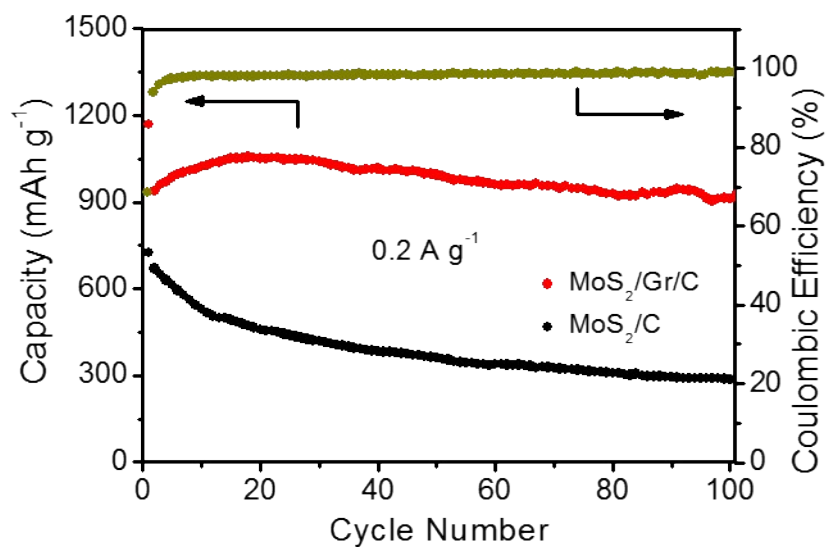


**Fig. S4** The cycling stability of $MoS_2/Gr/C$ and $MoS_2/C$ anodes at 0.2 A g$^{-1}$.
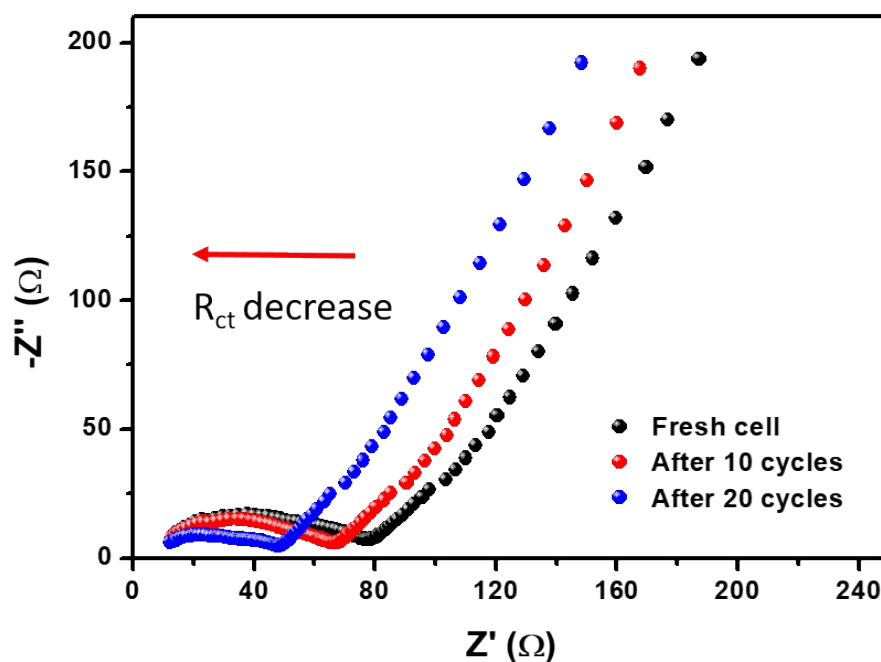
**Fig. S5** Nyquist plots of $MoS_2/Gr/C$ anode before and after 10, 20 cycles at 0.2 A $g^{-1}$.

It is well recognized that the phenomenon of capacity keeping increasing at the beginning in cycle test is generally attributed to the electrode activation through electrochemical reactions during charge-discharge. For our $MoS_2/Gr/C$ composite, the vertical channels can effectively shorten the pathway of Li-ion diffusion, providing larger contact areas of active materials with electrolyte, guaranteeing the full activation of electrodes; meanwhile, the expanded interlayer spacing not only enhances the kinetics of $Li^+$ intercalation/deintercalation, but also buffers the volume change during this process. Thus, this novel structure can simultaneously ensure the full activation and structural stability of electrodes.

To verify this, we have conducted the EIS test at first 20 cycles in cycling test at 0.2 A $g^{-1}$. The impedance was measured every ten cycles. As shown in Fig. S5, the charge transfer resistance ($R_{ct}$) decreases with the increasing number of cycles, proving the full activation of electrodes and excellent structural stability. These results are consistent with the phenomenon that the capacity increases firstly as the cycle number increasing at 0.2 A/g.
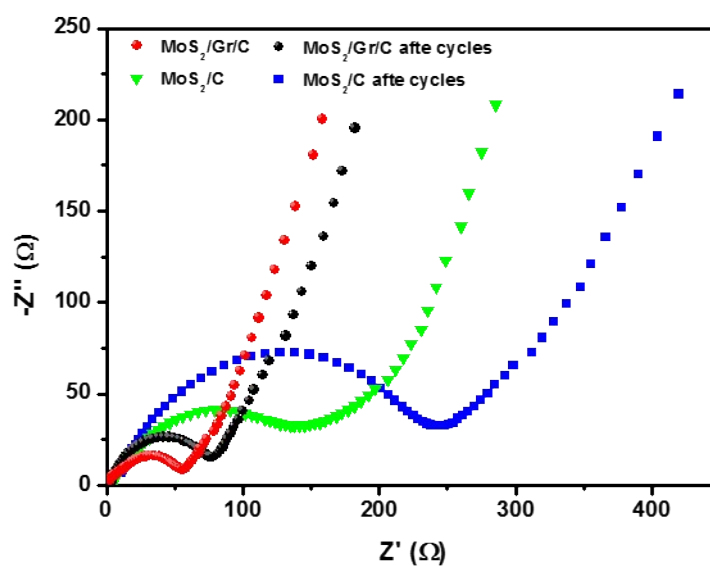
**Fig. S6** Nyquist plots of $MoS_2/Gr/C$ and $MoS_2/C$ anodes before and after 100 cycles at 0.2 A $g^{-1}$.

As shown in Fig. S6 the charge transfer resistances ($R_{ct}$, the diameter of semicircle at high frequency) of $MoS_2/Gr/C$ and $MoS_2/C$ anodes are 52.9 and 131.6 $\Omega$, respectively, indicating that $MoS_2/Gr/C$ has higher conductivity due to the existence of graphene. After 100 cycles at 0.2 A $g^{-1}$, $R_{ct}$ of $MoS_2/Gr/C$ only increases to 74.2 $\Omega$, much smaller than that of $MoS_2/C$ (233 $\Omega$), suggesting a better structure stability for the $MoS_2/Gr/C$ anode.
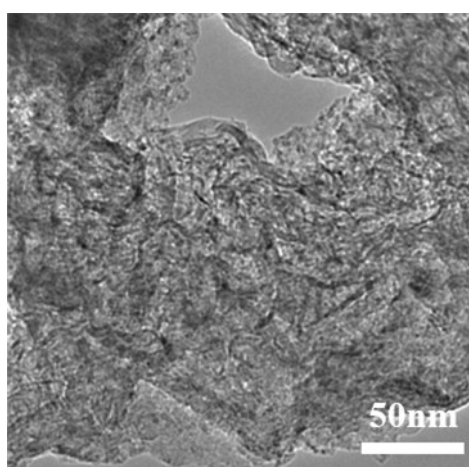


**Fig. S7** TEM image of the $MoS_2/Gr/C$ composite after 100 cycles at 0.2 A $g^{-1}$.
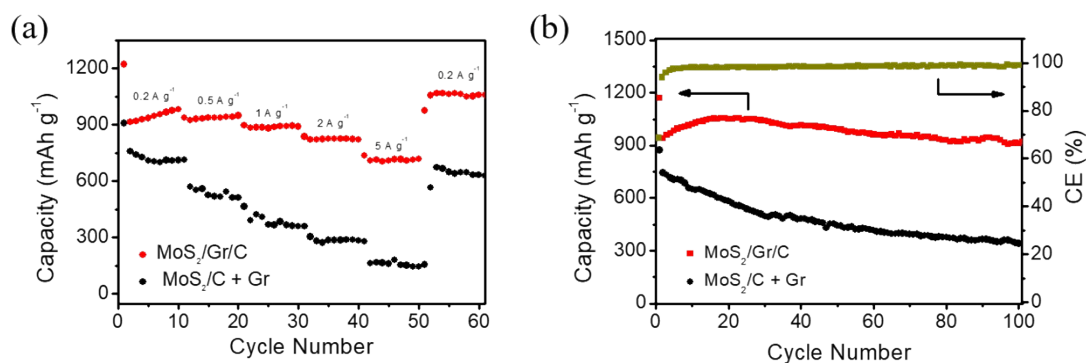
**Fig. S8** (a) The rate performance of $MoS_2/Gr/C$ and $MoS_2/C+Gr$ anodes. (b) The cycling stability of $MoS_2/Gr/C$ and $MoS_2/C+Gr$ anodes at 0.2 A $g^{-1}$.

In our work, the graphene is not only the conductive skeleton, but also the key to the vertical growth of $MoS_2$ crystals. Without graphene, the $MoS_2$ nanosheets in $MoS_2/C$ composite are randomly stacked in the flower-like form, instead of vertical structure. To distinguish the influence of the vertical channel and the other advantages of graphene (such as good electrical conductivity, high specific surface area), we have compared the electrochemical performance of the two samples. The one is our $MoS_2/Gr/C$ composite, the other is $MoS_2/C+Gr$ (mechanical mixing the $MoS_2/C$ composite and commercial graphene (The Sixth Element Inc.) in proportion), which guarantees that the control sample has other advantages of graphene but not including the vertical structure.

Fig. S8 shows that the electrochemical performance of $MoS_2/C+Gr$ are much lower than those of $MoS_2/Gr/C$. As shown in Fig. S8a, the $MoS_2/C+Gr$ anode delivers average specific capacities of 725.5, 518.3, 366.6, 289.1, 166.3, and 645.1 mAh $g^{-1}$ at 0.2, 0.5, 1, 2, 5, and 0.2 A $g^{-1}$, respectively, indicating the poor rate performance. Fig. S8b shows the poor cycling performance of $MoS_2/C+Gr$, retaining only 45.7% (339.7 mAh $g^{-1}$) of the capacity in the second cycle. Through such control experiments, we can determine that the main reason of the superior performance lies in the stable vertical channel structure of $MoS_2/Gr/C$, rather than the introduction of graphene.
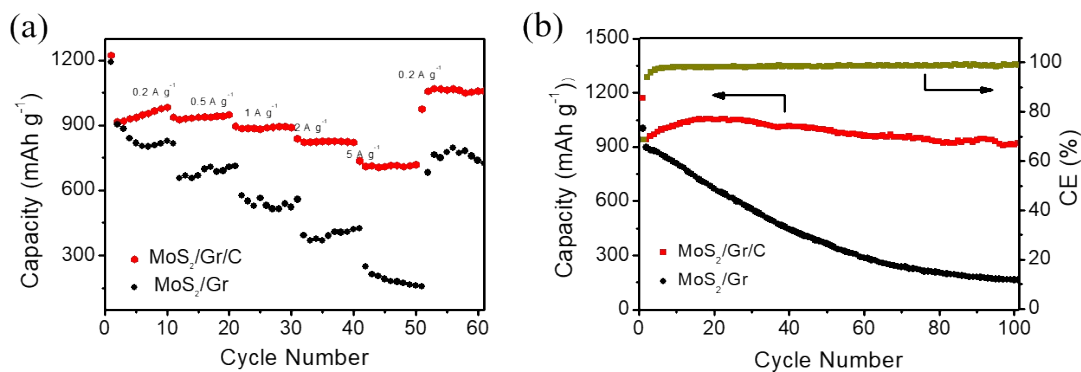
**Fig. S9** (a) The rate performance of $MoS_2/Gr/C$ and $MoS_2/Gr$ anodes. (b) The cycling stability of $MoS_2/Gr/C$ and $MoS_2/Gr$ anodes at 0.2 A g⁻¹.

The poor electrochemical performance of $MoS_2/Gr$ is presented in Fig. S9. Fig. S9a shows that the $MoS_2/Gr$ anode delivers average specific capacities of 883.7, 685.9, 530.3, 375.9, 177.9, and 749.0 mAh g⁻¹ at 0.2, 0.5, 1, 2, 5, and 0.2 A g⁻¹, respectively, indicating the poor rate performance. Fig. S9b shows the poor cycling performance of $MoS_2/Gr$, retaining only 18.2% (163 mA h g⁻¹) of the capacity in the second cycle.
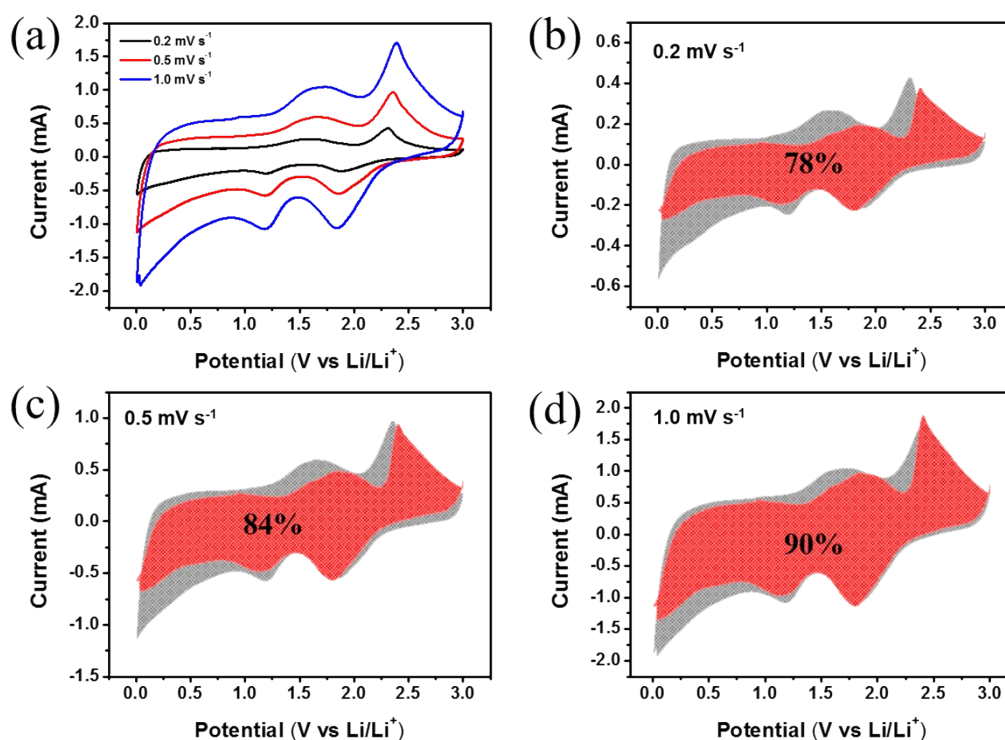


**Fig. S10** (a) CV curves of $MoS_2/Gr/C$ anode at scan rate of 0.2, 0.5, and 1.0 mV s⁻¹, respectively. Capacitive contribution of $MoS_2/Gr/C$ at a scan rate of (b) 0.2 mV s⁻¹, (c) 0.5 mV s⁻¹, and (d) 1 mV s⁻¹.
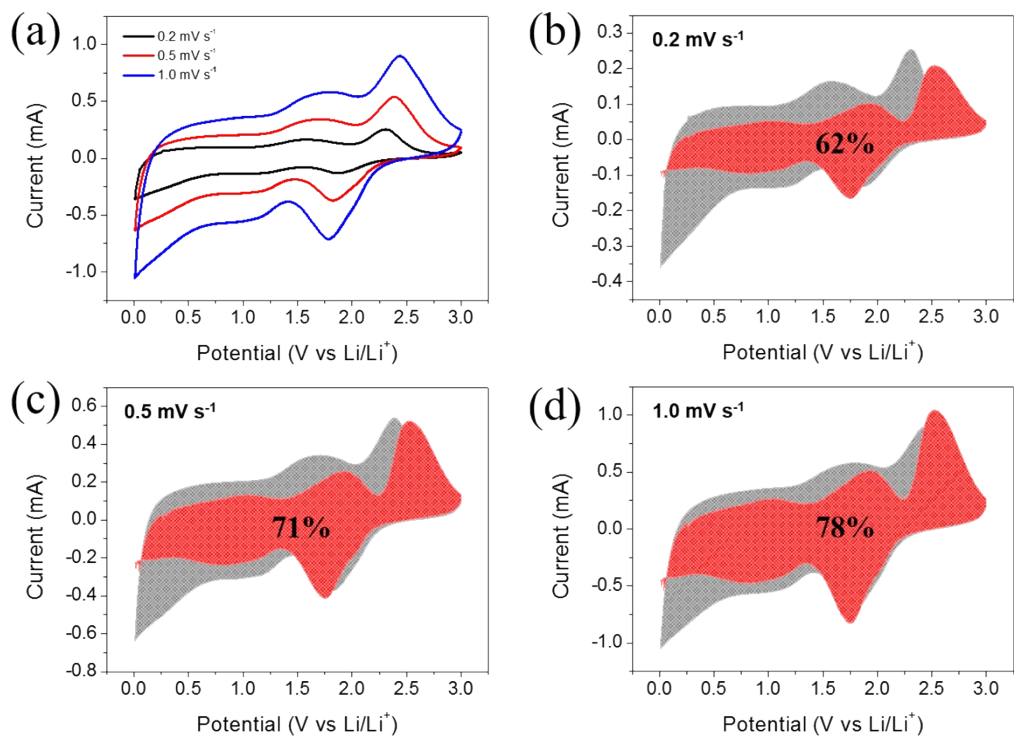
**Fig. S11** (a) CV curves of MoS$_2$/C anode at scan rate of 0.2, 0.5, and 1.0 mV s$^{-1}$, respectively. Capacitive contribution of MoS$_2$/C at a scan rate of (b) 0.2 mV s$^{-1}$, (c) 0.5 mV s$^{-1}$, and (d) 1 mV s$^{-1}$.
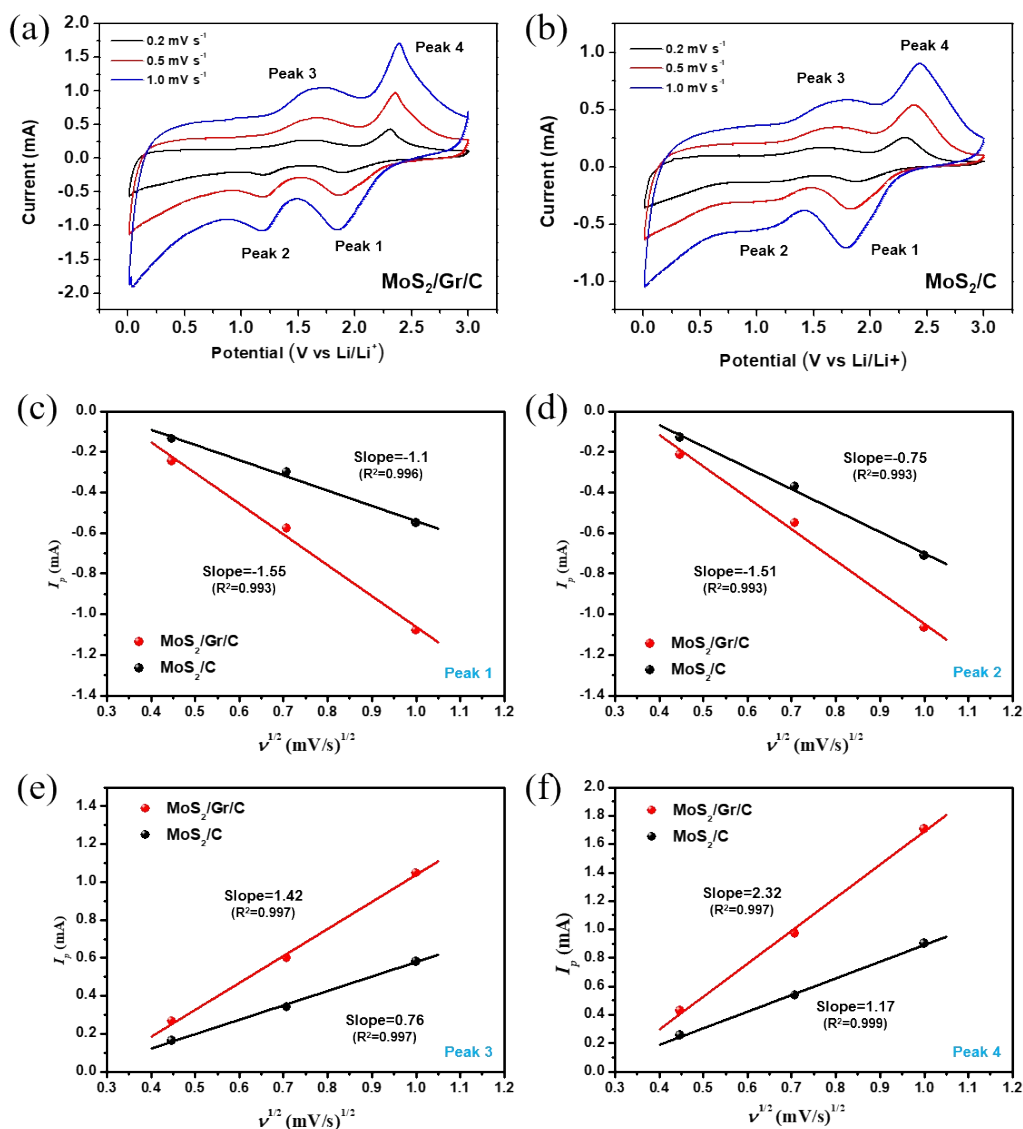
**Fig. S12** (a, b) CV curves of MoS₂/Gr/C and MoS₂/C anodes at scan rate of 0.2, 0.5, and 1.0 mV s⁻¹. (c-f) The plots of $I_p$-$\upsilon^{1/2}$ extracted from all 4 peak currents in the CV curves of MoS₂/Gr/C and MoS₂/C electrodes.

To further confirm the enhanced kinetic in MoS₂/Gr/C, we have used Randles-Sevcik equation (equation 1) to obtain the information about lithium-ion diffusion coefficients in both cells.

For both cells, it was found that the peak current ($I_p$/mA) were proportional to the square root of scan rate $\upsilon$ (Fig. S12c-f). This indicates the oxidation/reduction reaction is reversible. The relationship between $I_p$ and $\upsilon$ as follows:

$$I_p = 2.69 \times 10^5 \, n^{3/2} \, A D^{1/2} \upsilon^{1/2} C \qquad (1)$$

where n is the number of electrons transferred per molecule, A is the active surface area of the electrode, and C is the initial concentration of lithium ions in electrode, which are deemed to be the same for $MoS_2/Gr/C$ and $MoS_2/C$, and D is the $Li^+$ diffusion coefficient.

From eq. 1, we can conclude that the electrochemical reaction is more efficient (lithium ions diffuse faster) in the electrode when the slope of the plot of $I_p$-$\upsilon^{1/2}$ is larger. We analyzed all 4 peak currents ($I_p$) in the CV curves of $MoS_2/Gr/C$ and $MoS_2/C$ electrodes (Fig. S12a, b). The results (Fig. S12c-f, Table S1) show that all slopes of the plot of $I_p$-$\upsilon^{1/2}$ in $MoS_2/Gr/C$ are larger than those in $MoS_2/C$, which substantiates the enhanced kinetics in $MoS_2/Gr/C$.

**Table S1.** The slopes of $I_p$-$\upsilon^{1/2}$ in $MoS_2/Gr/C$ and $MoS_2/C$ electrodes.

| Corresponding Peak | Slope $MoS_2/Gr/C$ | Slope $MoS_2/C$ |
|---|---|---|
| Peak 1 | -1.55 | -1.1 |
| Peak 2 | -1.51 | -0.75 |
| Peak 3 | 1.42 | 0.76 |
| Peak 4 | 2.32 | 1.17 |

**Table S2** Comprehensive comparison of electrochemical performances among the MoS$_2$/Gr/C anode and the latest reported results in MoS$_2$-based Li-ion batteries.

| Typical materials | Rate performance (mAh g$^{-1}$, at low current) | Rate performance (mAh g$^{-1}$, at high current) | Cycling stability (mAh g$^{-1}$/ Cycles) | Decay rate per cycle (%) | Reference |
|---|---|---|---|---|---|
| **MoS$_2$/Gr/C** | **1051.2 (0.2 A g$^{-1}$)** | **712.1 (5 A g$^{-1}$)** | **921.7/100 (0.2 A g$^{-1}$)** | **0.019** | *This work* |
| | | | **525/1000 (5 A g$^{-1}$)** | **0.02** | |
| GF@CNT@MoS$_2$ | 925 (0.1 A g$^{-1}$) | 229 (5 A g$^{-1}$) | 506/200 (0.2A g$^{-1}$) | ~0.25 | [1] |
| MoS$_2$/N–C NWs | 880 (0.1 A g$^{-1}$) | 600 (5 A g$^{-1}$) | 821/100 (0.1A g$^{-1}$) 520/500 (5 A g$^{-1}$) | -- ~0.032 | [2] |
| MoS$_2$/ C-0.3 | 820 (0.1 A g$^{-1}$) | 530 (5 A g$^{-1}$) | 833/100 (0.1 A g$^{-1}$) | 0.019 | [3] |
| MoS$_2$/C-CPM | 832 (0.1 A g$^{-1}$) | 344 (2 A g$^{-1}$) | 831/220 (0.2 A g$^{-1}$) | 0.037 | [4] |
| MoS$_2$/N-C | ~1100 (0.1 A g$^{-1}$) | 895 (1 A g$^{-1}$) | 1102/100 (0.1 A g$^{-1}$) | 0.36 | [5] |
| MoS$_2$/GA–GF | 993 (0.2 A g$^{-1}$) | 595 (5 A g$^{-1}$) | 843/500 (1 A g$^{-1}$) | -- | [6] |
| MoS$_2$@N-CF | 965 (0.2 A g$^{-1}$) | 702 (4 A g$^{-1}$) | 844/110 (1 A g$^{-1}$) | -- | [7] |
| 8.4%C-MoS$_2$ | 970 (0.1 A g$^{-1}$) | 710 (1 A g$^{-1}$) | ~900/100 (1 A g$^{-1}$) | 0.027 | [8] |
| MoS$_2$ NT@C | 983 (0.1 A g$^{-1}$) | 650 (3 A g$^{-1}$) | 1106/150 (0.1 A g$^{-1}$) | -- | [9] |
| MoS$_2$-C-RGO | 759 (0.1 A g$^{-1}$) | ~450 (5 A g$^{-1}$) 375 (10 A g$^{-1}$) | 600/300 (1 A g$^{-1}$) | -- | [10] |

**References:**

[1] J. Ren, R. Ren, Y. Lv, *Chem. Eng. J.,* **2018**, *353*, 419.

[2] H. Sun, J. Wang, Y. Zhang, W. Hua, Y. Li, H. Liu, *J, Mater. Chem. A,* **2018**, *6*, 13419.

[3] T. Yang, J. Liang, I. Sultana, M. M. Rahman, M. J. Monteiro, Y. I. Chen, Z. Shao, S. R. P. Silva, J. Liu, *J, Mater. Chem. A,* **2018**, *6*, 8280.

[4] B. Chen, H. Lu, N. Zhao, C. Shi, E. Liu, C. He, L. Ma, *J. Power Sources,* **2018**, *387*, 16.

[5] Z. Lei, L. Xu, Y. Jiao, A. Du, Y. Zhang, H. Zhang, *Small,* **2018**, *14*, 1704410.

[6] W. Wang, P. Yang, Z. Jian, H. Li, Y. Xing, S. Zhang, *J, Mater. Chem. A,* **2018**, *6*, 13797.

[7] Z. Miao, P. Wang, Y. Xiao, H. Fang, L. Zhen, C. Xu, *ACS Appl. Mater. Interfaces,* **2016**, *8*, 33741.

[8] W. Sun, Z. Hu, C. Wang, Z. Tao, S. Chou, Y. Kang, H. Liu, *ACS Appl. Mater. Interfaces,* **2016**, *8*, 22168.

[9] F. Yi, Y. Niu, S. Liu, J. Hou, S. Bao, M. Xu, *Phys. Chem. Chem. Phys.,* **2016**, *18*, 19792.

[10] R. Wang, S. Wang, D. Jin, Y. Zhang, Y. Cai, J. Ma, L. Zhang, *Energy Storage Mater.,* **2017**, *9*, 195.